



Cite this: *J. Mater. Chem. A*, 2022, **10**, 9707

## An efficient screening strategy towards multifunctional catalysts for the simultaneous electroreduction of $\text{NO}_3^-$ , $\text{NO}_2^-$ and NO to $\text{NH}_3$ †

Peng Lv,<sup>a</sup> Donghai Wu,<sup>a</sup> Bingling He,<sup>a</sup> Xue Li,<sup>a</sup> Rui Zhu,<sup>a</sup> Gang Tang,<sup>b</sup> Zhansheng Lu,<sup>c</sup> Dongwei Ma,<sup>a</sup> \*<sup>a</sup> and Yu Jia,<sup>a</sup> \*<sup>a</sup>

Multifunctional electrocatalysts that simultaneously reduce all  $\text{NO}_x$  species ( $\text{NO}_3^-$ ,  $\text{NO}_2^-$  and NO) to  $\text{NH}_3$  can deliver superior efficiency compared with that for individual species. Herein, by using the first-principles method, an efficient strategy was proposed to screen  $\text{NO}_x\text{RR}$  multifunctional electrocatalysts, which focuses on the key protonation process of the essential NORR for the  $\text{NO}_x\text{RR}$ . Taking double-atom catalysts (DACs) with transition-metal dimer ( $\text{M}_1/\text{M}_2 = \text{V, Cr, Mn, Fe, Co, Ni, and Cu}$ ) embedded N-doped graphene as examples, we showed that the proposed strategy was effective for electrocatalyst screening, and we identified  $\text{Cu}_2@\text{NG}$  as the best one, with rather low limiting potentials of  $-0.36$ ,  $-0.32$ , and  $-0.30$  V for the  $\text{NO}_3\text{RR}$ ,  $\text{NO}_2\text{RR}$ , and NORR, respectively. Furthermore, a simple descriptor for evaluating electrocatalytic activity was established. And the physical mechanism in terms of the electronic structures was analyzed for the  $\text{Cu}_2$  DAC case in view of NO activation. Finally, from the screening test in some 4d and 5d late transition-metal based DACs, the proposed strategy was confirmed to be feasible to find another  $\text{NO}_x\text{RR}$  multifunctional electrocatalyst. Our work provides a procedure for efficiently screening multifunctional electrocatalysts to simultaneously reduce all  $\text{NO}_x$  species to synthesize  $\text{NH}_3$  and sheds light on the atomic mechanisms for  $\text{NO}_x$  electroreduction as well.

Received 9th January 2022  
Accepted 19th March 2022

DOI: 10.1039/d2ta00192f  
[rsc.li/materials-a](http://rsc.li/materials-a)

## 1. Introduction

For a long time, the production of valuable ammonia ( $\text{NH}_3$ ) mainly has depended on the traditional Haber–Bosch process that occurs at high temperature and pressure and is extremely economically and environmentally unfriendly. Yet, researchers turned to the electrochemical  $\text{N}_2$  reduction reaction (NRR) mimicking biological nitrogen fixation towards  $\text{NH}_3$ .<sup>1–6</sup> Due to the poor NRR performance resulting from the extremely inert  $\text{N}\equiv\text{N}$  bond, alternatively the electrochemical conversion of other important nitrogenous species,  $\text{NO}_x$  ( $\text{NO}_3^-$ ,  $\text{NO}_2^-$  and NO), came into focus very recently. It turns out that this not only produces  $\text{NH}_3$  beyond NRR under ambient conditions, but also removes the waste  $\text{NO}_x$  species.<sup>7,8</sup> In contrast, this

denitrification process in nature reduces the  $\text{NO}_x$  species to  $\text{N}_2\text{O}$  by fungi and  $\text{N}_2$  by bacteria.<sup>9</sup>

It should be noted that nitrate and nitrite ions usually coexist in waste water, such as contaminated groundwater, lakes, and coastal water, which also includes NO from biological denitrification.<sup>9</sup> In addition, the  $\text{NO}_x$  species can be easily obtained by the plasma activation of air.<sup>10,11</sup> To this end, developing multifunctional electrocatalysts that simultaneously reduce all the  $\text{NO}_x$  species promises higher conversion efficiency for  $\text{NH}_3$  synthesis compared with monofunctional ones.<sup>10,12,13</sup> Up to now, existing research has mainly focused on monofunctional systems for individual species, while the design strategy of multifunctional catalysts for the  $\text{NO}_x\text{RR}$  has been lacking. As we all know, the NORR is an essential reaction for determining the performance of electrocatalysts for the electroreduction of  $\text{NO}_3^-$  and  $\text{NO}_2^-$  to  $\text{NH}_3$ .<sup>14,15</sup> Therefore, for the  $\text{NO}_x\text{RR}$  towards  $\text{NH}_3$  instead of other by-products ( $\text{H}_2$ ,  $\text{N}_2$ , and  $\text{N}_2\text{O}$ ), the premise is to design an efficient NORR electrocatalyst with high activity and  $\text{NH}_3$  selectivity.

Since the proposal of single-atom catalysts (SACs) by Zhang *et al.* in 2011,<sup>16</sup> they have also been confirmed to show high activity for  $\text{NH}_3$  synthesis from the NORR,  $\text{NO}_2\text{RR}$  or  $\text{NO}_3\text{RR}$  (*i.e.*,  $\text{Mg}/\text{Al}/\text{Ga}/\text{Co}@\text{NG}$ ,<sup>17–19</sup>  $\text{Zr}-\text{C}_2\text{N}$ ,<sup>20</sup>  $\text{Ru}@\text{C}_3\text{N}_4$ ,<sup>21</sup> and  $\text{Ti}/\text{Zr}@\text{CN}$ ).<sup>22</sup> Unfortunately, the individual active site gives rise to their deficiency in multifunctional electrocatalytic ability to reduce all the  $\text{NO}_x$  species, which motivates us to design

<sup>a</sup>Key Laboratory for Special Functional Materials of Ministry of Education, School of Materials Science and Engineering, Henan University, Kaifeng 475004, China. E-mail: madw@henu.edu.cn; jiayu@henu.edu.cn

<sup>b</sup>Advanced Research Institute of Multidisciplinary Science, Beijing Institute of Technology, Beijing 100081, China

<sup>c</sup>School of Physics, Henan Normal University, Xinxiang 453007, China

<sup>d</sup>International Laboratory for Quantum Functional Materials of Henan, School of Physics, Zhengzhou University, Zhengzhou 450001, China

<sup>e</sup>Joint Center for Theoretical Physics, Center for Topological Functional Materials, Henan University, Kaifeng 475004, China

† Electronic supplementary information (ESI) available. See DOI: 10.1039/d2ta00192f

multifunctional electrocatalysts. Given the flexibility of dual active sites in double-atom catalysts (DACs),<sup>23–26</sup> there are more possibilities to adjust their geometrical bridge configurations,<sup>27</sup> offering more opportunities to modulate the binding strength of reaction intermediates and then optimize the catalytic activity, selectivity and multifunctional ability.<sup>28</sup> For instance, compared with atomically dispersed single Fe and Ni catalysts, with the help of the synergistic effect of dual active sites, a bimetallic FeNi DAC exhibits outstanding multifunctional performance for the reversible oxygen evolution reaction and oxygen reduction reaction.<sup>29</sup> Furthermore, various DACs have been theoretically and experimentally confirmed to show high activity and selectivity for the NRR.<sup>23,30–35</sup> In view of these advantages, it is expected that DACs would be multifunctional electrocatalysts with the potential ability for reducing all  $\text{NO}_x$  species, which has not yet been reported.

Here, by using the first-principles method, we proposed an optimized strategy for screening multifunctional electrocatalysts to reduce all  $\text{NO}_x$  species. The screening strategy consists of the steps of “stability of catalyst”, “NO adsorption”, “NORR activity”, and “ $\text{NH}_3$  selectivity”. We used the selection metric of “two steps of key hydrogenation process” to measure the “NORR activity”, which is confirmed to be very effective. According to some late transition-metal based SACs with good electrocatalytic ability for the  $\text{NO}_2\text{RR}$  or  $\text{NO}_3\text{RR}$  in the experiment,<sup>18,36–38</sup> together with recently synthesized transition-metal dimer embedded N-doped graphene (M1M2@NG),<sup>32,39–43</sup> 28 DAC candidates were built (M1/M2 = V, Cr, Mn, Fe, Co, Ni, and Cu) for screening multifunctional electrocatalysts for the  $\text{NO}_x\text{RR}$ . Through firstly systematic screening for NORR electrocatalysts, the DAC of  $\text{Cu}_2\text{@NG}$  was identified as the best one due to its smallest limiting potential ( $U_L$ ,  $-0.30$  V) and high  $\text{NH}_3$  selectivity. As expected, the catalytic merits of  $\text{Cu}_2\text{@NG}$  can be extended to the  $\text{NO}_2\text{RR}$  ( $U_L$ ,  $-0.36$  V) and  $\text{NO}_3\text{RR}$  ( $U_L$ ,  $-0.32$  V). Moreover, the electroreduction activity descriptor and physical mechanism in terms of electronic structures were analyzed. Our work provides an effective strategy to screen multifunctional electrocatalysts for the  $\text{NO}_x\text{RR}$ , by which a cost-efficient and stable candidate with desirable  $\text{NH}_3$  activity and selectivity was identified.

## 2. Methods

All spin-polarized computations were carried out by the generalized gradient approximation (GGA) method with the Perdew–Burke–Ernzerhof (PBE) functional<sup>44</sup> based on density functional theory (DFT) implemented in the Vienna *ab initio* simulation package (VASP),<sup>45,46</sup> in which van der Waals (vdW) correction proposed by Grimme (DFT+D3) was chosen.<sup>47</sup> The plane-wave basis set with a cut-off energy of 450 eV was employed. The convergence thresholds of the total energy and the Hellmann–Feynman force are  $10^{-5}$  eV and  $0.02$  eV  $\text{\AA}^{-1}$ , respectively. A  $7 \times 7$  supercell of graphene with a vacuum layer of  $\sim 18$   $\text{\AA}$  is used to avoid the interactions between periodic images for all calculations. Monkhorst–Pack meshes of  $3 \times 3 \times 1$  and  $7 \times 7 \times 1$  are adopted for structural optimization and calculation of densities of states (DOS), respectively.

The free energy change ( $\Delta G$ ) under the acidic medium (pH = 0) for each elementary reaction step was calculated based on the computational hydrogen electrode (CHE) model,<sup>48–50</sup> according to the following equation:

$$\Delta G = \Delta E + \Delta E_{\text{ZPE}} - T\Delta S$$

$\Delta E$  is the reaction energy from DFT calculations.  $\Delta E_{\text{ZPE}}$  and  $T\Delta S$  ( $T = 298.15$  K) are the contributions of the zero-point energy and entropy to  $\Delta G$ , respectively.  $E_{\text{ZPE}}$  and  $TS$  for the free molecules are taken from the NIST database,<sup>51</sup> and those of the adsorbed species were obtained based on the calculated vibrational frequencies and then with the VASPKIT code.<sup>52</sup> The limiting potential ( $U_L$ ) is defined as  $-\Delta G_{\text{max}}/e$ , where  $\Delta G_{\text{max}}$  is the free energy change of the potential-determining step (PDS). Due to the difference of formation energies from experimental and DFT results for  $\text{HNO}_3$  and  $\text{HNO}_2$ , along with the energy difference of solvated  $\text{NO}_3^-/\text{NO}_2^-$  (aq) and  $\text{HNO}_3/\text{HNO}_2$  (g), here  $\Delta G(\text{NO}_3^-)$  and  $\Delta G(\text{NO}_2^-)$  are correspondingly corrected based on their differences.

The hybrid model,<sup>53,54</sup> *i.e.*, the combination of explicit solvation model with two water molecules near the active site and continuum solvation model,<sup>55</sup> was used to investigate the solvation effect on the  $\text{NO}_x\text{RR}$ . The solvation effect doesn't change our conclusions about the screening of multifunctional electrocatalysts for the  $\text{NO}_x\text{RR}$  (for the details and results, see Note S1 in the ESI†). The pH effect was also considered from the viewpoints of thermodynamics and dynamics. The results show that  $\text{Cu}_2$  and  $\text{Ag}_2$  DACs are excellent acidic electrocatalysts to multifunctionally reduce all the  $\text{NO}_x$  species (for the details and results, see Note S2 in the ESI†). The thermal stability of  $\text{Cu}_2$  and  $\text{Ag}_2$  DACs was examined by *ab initio* molecular dynamics simulations<sup>56</sup> for 10 ps with the current  $7 \times 7$  supercells of graphene (for the details and results, see Note S3 in the ESI†).

## 3. Results and discussion

For DACs, graphene containing nitrogen (NG) is an excellent substrate with anchoring sites for metal dimer deposition. Some DACs of  $\text{Fe}_2\text{@NG}$ ,<sup>39</sup>  $\text{FeCo}\text{@NG}$ ,<sup>40,41</sup>  $\text{FeNi}\text{@NG}$ ,<sup>24</sup> and  $\text{CoNi}\text{@NG}$ <sup>42</sup> have been definitely determined experimentally and exhibit excellent catalytic performances for the  $\text{O}_2$  reduction reaction (ORR). In addition, a few M1M2@NG DACs also possess a great  $\text{N}_2$  reduction ability with  $\text{NH}_3$  selectivity.<sup>5,32,43</sup> In this regard, M1M2@NG DACs may be promising electrocatalyst candidates for the  $\text{NO}_x\text{RR}$  including both the hydrogenation of N and O atoms in the  $\text{NO}_x$  species. Given that the NORR is the essential reaction of the  $\text{NO}_x\text{RR}$ , we will firstly consider the design of a NORR electrocatalyst from the M1M2@NG system. The atomic structure of M1M2@NG is presented in Fig. 1a, where each metal atom is tetra-coordinated with three N atoms and another metal atom. Both the homonuclear and heteronuclear cases were considered for 3d metals (M1/M2 = V, Cr, Mn, Fe, Co, Ni, and Cu), leading to 28 kinds of DAC candidates. The deposited metal dimers are well within the atomic plane of graphene, probably thanks to the large size of the pore decorated with the edge N atoms. Our recent studies<sup>5,34</sup> showed that

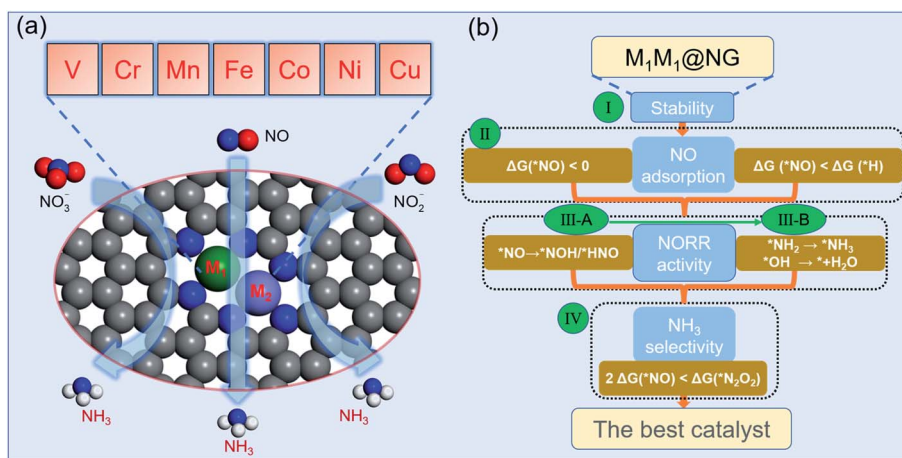


Fig. 1 (a) The atomic structure of M1M2@NG DACs (M1/M2 = V, Cr, Mn, Fe, Co, Ni, and Cu). (b) The optimized strategy for screening NORR electrocatalysts including four stepwise selection principles. The third criterion consists of “two steps of key hydrogenation process”.

the metal dimer in DACs can provide a bridge active site for the adsorption of  $\text{N}_2$  and relevant intermediates, which is beneficial for molecular activation and its further hydrogenation.

According to the NORR characteristics,<sup>12,18,57-59</sup> we comprehensively proposed four stepwise selection principles (Fig. 1b) for the best NORR electrocatalysts: (I) the thermodynamic stability of the catalyst for the feasibility of experimental realization, (II) stable adsorption of molecular NO for activation, and superiority to H, (III) high NORR activity to  $\text{NH}_3$  with low  $\Delta G_{\text{max}}$  (here the threshold value ( $G_T$ ) was set as 0.4 eV, *i.e.*,  $U_L \geq 0.4$  V), and (IV) great  $\text{NH}_3$  selectivity with inhibitive ability of other products ( $\text{N}_2$  and  $\text{N}_2\text{O}$ ).<sup>14</sup> Particularly, for the third criterion, we used the selection metric of “two steps of key hydrogenation process” to measure the catalytic activity for the NORR, rather than calculating the overall reaction pathway of numerous candidates.

We have investigated the feasibility of experimental realization of these 28 DACs based on the calculated formation energies and binding energies.<sup>5</sup> The results showed that their formation energies (about 2.8–4.3 eV) are lower than or comparable with those of several synthesized ones (*i.e.* FeNi@NG,<sup>24</sup> Fe<sub>2</sub>@NG,<sup>39</sup> FeCo@NG,<sup>40,41</sup> and CoNi@NG<sup>42</sup>). And their more negative binding energies (about –9.5 to –13.5 eV) suggest that highly stable complexes can be formed by depositing metal atoms onto an N-doped porous graphene support. As the first step of the NORR, the adsorption and activation of NO on M1M2@NG DACs were investigated. Various kinds of NO adsorption configurations were initially studied to determine the favorable one. The most stable adsorption configurations are summarized in Fig. S1.† It was found that most stable species over M1M2@NG prefer to stay over the metal atoms with three representative configurations (Fig. 2a): (1) the side-on pattern with the N atom binding with both metal atoms and the O atom with one metal atom ( $\text{NO}^\alpha$ ), and (2) the end-on pattern with the N atom binding with both metal atoms ( $\text{NO}_{\text{M1M2}}^\beta$ ) or one metal atom ( $\text{NO}_{\text{M1}}^\beta$ ).

Interestingly, most DACs adopt an end-on configuration for  $\text{NO}$  ( $\text{NO}_{\text{M1}}^\beta$  mainly for Ni and Cu-alloy DACs), while only V<sub>2</sub>,

VCr, and VMn@NG DACs prefer to adopt the side-on  $\text{NO}^\alpha$  configuration (Fig. S1.†), which may result from the fact that V<sub>2</sub>, VCr, and VMn dimers have fewer d-orbital electrons. From the relationship between the charge transfer ( $Q$ , e) and N–O bond length in Fig. 2b, the side-on  $\text{NO}^\alpha$  configurations transfer more electrons (1.00–1.04 e) from the DAC support to the  $\text{NO}^\alpha$  and make the length of the N–O bond longer (1.35–1.38 Å from 1.15 Å in the free NO molecule). For each  $\text{NO}_{\text{M1}}^\beta$  and  $\text{NO}_{\text{M1M2}}^\beta$  end-on configuration, there is a nearly linear correlation between the electron transfer and the length of the N–O bond. Correspondingly, the  $\text{NO}_{\text{M1}}^\beta$  configurations have relatively less electron transfer between the  $\text{NO}^\alpha$  and DACs than  $\text{NO}_{\text{M1M2}}^\beta$  configurations, resulting in the difference of N–O bond lengths. From the free energy change for  $\text{NO}$  (Fig. 2c), we can find that  $\text{NO}^\alpha$  over V<sub>2</sub>, VCr, and VMn DACs with a side-on configuration has smaller  $\Delta G$  values due to the higher activation of  $\text{NO}^\alpha$  with a large N–O bond length than that with an end-on configuration. Moreover, all the DACs have negative  $\Delta G$  values for  $\text{NO}^\alpha$  with enlarging N–O bond, indicating the chemical adsorption and activation of  $\text{NO}^\alpha$ . The negative  $\Delta G$  has a linear relationship with the total number of d-orbital valence electrons ( $N_{\text{d-orbital}}$ ) of free metal-dimer atoms (Fig. S2.†): more  $N_{\text{d-orbital}}$  corresponds to less negative  $\Delta G$ . Thus, the Cu<sub>2</sub> DAC has the least negative  $\Delta G$  for the NO configuration among these DAC systems, while it still possesses the capture ability for NO molecules under ambient conditions.

Since H adsorption is generally strong on most bulk metal surfaces, the active site of metal surfaces can be easily blocked by the covered  $\text{H}$  to inhibit electrocatalytic reduction, such as for the NRR.<sup>60</sup> Here also for the NORR, NO adsorption has to compete with the H adsorption over active sites. Based on this, we calculated the H adsorption on various DACs and the comparison results of  $\Delta G(\text{H})$  and  $\Delta G(\text{NO})$  are organized in Fig. 2d. We found that all the electrocatalysts have more negative  $\Delta G$  values for  $\text{NO}^\alpha$  than that for  $\text{H}$  over the corresponding DACs, indicating that they have a strong binding capability for NO to suppress the competing HER.

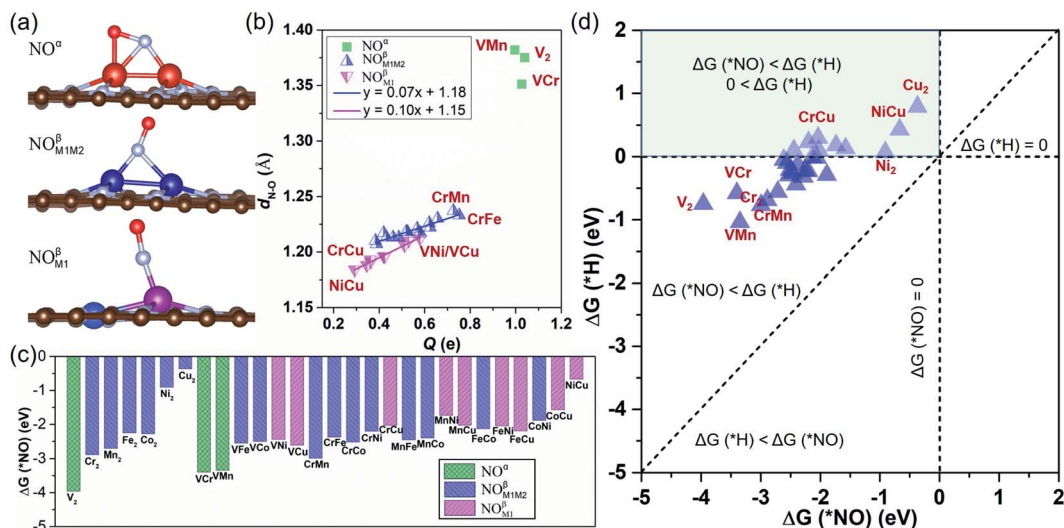


Fig. 2 (a) Side views of the three most stable adsorption configurations of NO over M1M2@NG DACs. (b) The relationship between the charge transfer ( $Q$ , e) and the N–O bond length ( $d_{N–O}$  (\*NO), Å) of the most favorable \*NO configurations on each M1M2@NG. Here, the positive values of  $Q$  indicate electron transfer from the catalyst to the adsorbed NO. (c) The free energy change ( $\Delta G$  (\*NO), eV) of the most stable \*NO configuration over various DACs. (d) The  $\Delta G$  for the \*NO and \*H over various DACs.

We then investigated the catalytic performances of the NORR over all DACs as most catalysts have a chemical adsorption ability for NO molecules. However, it's complex, cumbersome and resource-consuming work to consider all the reaction steps of the NORR for the 28 DACs that meet the first two rules (catalyst's stability and NO adsorption), which usually also occurred for other catalyst screening.<sup>5,34,43</sup> Thus, a one time and labor saving, and convenient method is an urgent need, which is significant for screening outstanding electrocatalysts for the NORR or multifunctional electrocatalysts for the  $NO_x$ RR.

From here obtained \*NO configurations and previous studies,<sup>19,57,61,62</sup> we summarized the detailed reaction pathways for the NORR towards  $NH_3$ , as shown in Fig. 3. Given that the NO molecule contains N and O atoms, the proton–electron pairs can attack the N atom and also the O atom to produce  $NH_3$  and  $H_2O$ , respectively. The sequential order of two product formation strongly depends on the NO adsorption configuration. Based on \*NO with an end-on configuration, the reaction can follow O/N-distal and -alternating mechanisms to firstly form the product  $H_2O$ . Correspondingly, the NO reduction follows O/N-consecutive and -enzymatic mechanisms to firstly form either  $H_2O$  or  $NH_3$ . In particular, under the side-on \*NO induced N-consecutive mechanism, protonation can lead to progressive hydrogenation of N atoms until  $NH_3$  is preferentially formed with O atoms left over active sites. Moreover, the different reaction mechanisms can convert or hybridize with each other. We can find that no matter what mechanism the reaction follows, the first hydrogenation step is the \*NOH/\*HNO formation from \*NO and the last hydrogenation step is the \* $NH_3$  or  $H_2O$  formation, indicating that the NORR includes both the NRR and ORR features.

According to the results from calculating the entire reaction steps in recent studies about the NORR<sup>19,61,62</sup> and the similarity to the NRR,<sup>32,63</sup> the PDS for the NORR towards  $NH_3$  may be the

stabilization of \*NOH/\*HNO species from NO adsorption (\*NO → \*NOH/\*HNO), or destabilization of \* $NH_2$  or \*OH species to form the products (\* $NH_2$  → \* $NH_3$ , or \*OH → \* +  $H_2O$ ). Thus, the third screening criterion (Fig. 1b) for NORR activity consists of “two steps of key hydrogenation process”, *i.e.*, (1) \*NO → \*NOH/\*HNO as the first procedure to select the catalyst candidates that meet the free energy threshold requirements (smaller than  $G_T$  of 0.40 eV) and (2) \* $NH_2$  → \* $NH_3$  or \*OH → \* +  $H_2O$  as the final procedure to confirm the NORR electrocatalyst with high activity. It is worth emphasizing that this reaction process always involves \* $NH_3$  and  $H_2O$  formation, whether in the middle or at the last step. We thus simplified the final screening procedure for NORR activity to a combination of \* $NH_2$  → \* $NH_3$  and \*OH → \* +  $H_2O$ .

From the calculated free energy change as depicted in Fig. 4a, we can find that the first hydrogenation step (\*NO → \*NOH/\*HNO) requires  $\Delta G$  smaller than  $G_T$  (0.40 eV) over eight DACs ( $V_2$ ,  $Cr_2$ ,  $Cu_2$ ,  $VCr$ ,  $VMn$ ,  $VFe$ ,  $VCu$ , and  $CrMn$ ), which are mostly V and Cr-based DACs (except for  $Cu_2$ ). Among these DACs, the chemical adsorption of \*NO upon hydrogenation forms stable intermediate \*HNO or \*NOH species with side-on configurations, except for  $VCu$  with an end-on configuration (Fig. S3†). The strong stabilization of \*HNO or \*NOH (only one for \*NOH over  $VCr$  DAC) is responsible for the high activity for the \*NO hydrogenation process. Here most of the DACs with small  $\Delta G$  give rise to the more favorable \*HNO than \*NOH, different from that over transition-metal borides with more favorable \*NOH.<sup>61</sup> Moreover, among these results, the N–O bond in \*NO can break spontaneously by hydrogenation under ambient conditions, causing the smallest  $\Delta G$  of the first hydrogenation step over  $V_2$  (−2.03 eV) and  $VCr$  (−1.68 eV) DACs.

Through the first round of preliminary screening for NORR activity, we thus calculated the free energy change of \* $NH_2$  → \* $NH_3$  and \*OH → \* +  $H_2O$  over the above eight DAC candidates

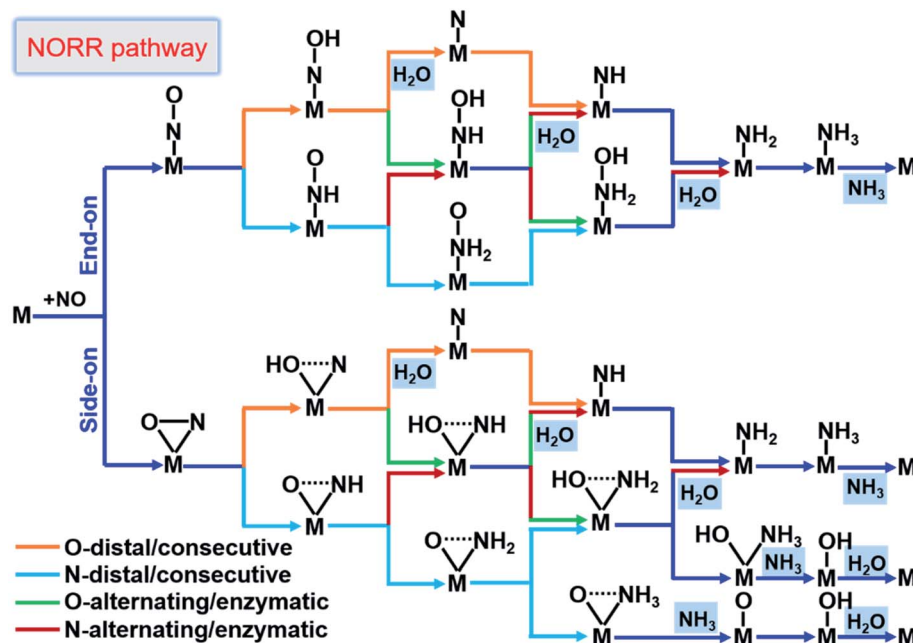


Fig. 3 Schematic depiction of the various pathways for the NORR towards  $\text{NH}_3$ . The dotted lines in the adsorbates indicate that bonds may be broken.

(Fig. 4b). It was found that only the  $\text{Cu}_2$  DAC meets the screening metric of  $\Delta G$  smaller than 0.4 eV, indicating that the  $\text{Cu}_2$  DAC may show the greatest electroactivity for the NORR towards  $\text{NH}_3$ . The other seven DACs have a larger  $\Delta G$  of  $\text{H}_2\text{O}$  formation (1.90 eV for  $\text{V}_2$ , 1.42 eV for  $\text{Cr}_2$ , 1.56 eV for  $\text{VCr}$ , 1.71 eV for  $\text{VMn}$ , 0.89 eV for  $\text{VFe}$ , 1.38 eV for  $\text{VCu}$ , and 1.10 eV for  $\text{VMn}$ ), which is greater than that for  $^*\text{NH}_3$  formation and leads to the poisoning of active sites of DACs by  $^*\text{OH}$  species. A similar poisoning phenomenon also occurs for  $\text{CO}_2$  reduction within low limiting potential for the Pd-based catalyst.<sup>64</sup>

A promising NORR electrocatalyst also requires good  $\text{NH}_3$  selectivity, which suggests that it should have the ability to suppress the competing reaction to form the by-product. For example, at high potential, the NORR will lead to by-product ( $\text{N}_2\text{O}$  or  $\text{N}_2$ ) formation on some metal surfaces.<sup>14</sup> For this reaction to occur, N–N coupling in the formation of  $\text{N}_2\text{O}_2$  is required from two NO co-adsorbed on one active site. In consequence, as the first step in initiating the whole competing reaction, the affinity to  $^*\text{NO}$  (towards  $\text{NH}_3$ ) and  $^*\text{N}_2\text{O}_2$  (towards  $\text{N}_2\text{O}$  and  $\text{N}_2$ ) on catalysts will give rise to their reduction selectivity

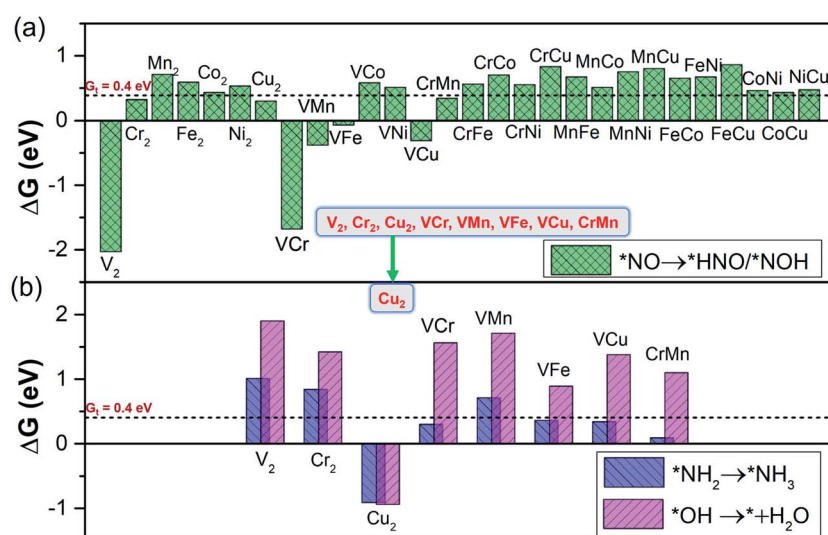


Fig. 4 The screening criterion of "two steps of key hydrogenation process" for NORR activity (step III in Fig. 1b), with the threshold value ( $G_T = 0.40$  eV). (a) The  $\Delta G$  for stabilization of  $^*\text{NOH}/^*\text{HNO}$  species ( $^*\text{NO} \rightarrow ^*\text{NOH}/^*\text{HNO}$ ) over the 28 DACs. (b) The  $\Delta G$  for destabilization of  $^*\text{NH}_2$  and  $^*\text{OH}$  species ( $^*\text{NH}_2 \rightarrow ^*\text{NH}_3$  and  $^*\text{OH} \rightarrow ^* + \text{H}_2\text{O}$ ) over the 28 DACs.

performance. We then compared their free energy changes for adsorption over the  $\text{Cu}_2$  DAC, *i.e.*,  $\Delta G$  ( ${}^*\text{N}_2\text{O}_2$ ) *vs.*  $\Delta G$  ( ${}^*\text{NO}$ ). It was found that the  ${}^*\text{N}_2\text{O}_2$  formation from the NO dimer by N–N bond coupling (Fig. S4†) is unfavorable due to its less negative  $\Delta G$  ( $-0.42$  eV) than that for two separated  ${}^*\text{NO}$  ( $-0.74$  eV). This indicates that the two  ${}^*\text{NO}$  prefer to separately adsorb on different active sites rather than on one site, which can suppress  $\text{N}_2\text{O}$  and  $\text{N}_2$  formation.

To elucidate the results and verify our screening rule for NORR activity, we obtained the free energy diagrams of the most relevant pathway (the other pathways are also considered) for the NORR under zero and applied potential over  $\text{Cu}_2$ ,  $\text{VCr}$ ,  $\text{VMn}$ ,  $\text{VFe}$ ,  $\text{VCu}$ , and  $\text{CrMn}$  DACs, all of which have  $\Delta G$  values smaller than  $0.4$  eV from  ${}^*\text{NH}_2$  to  ${}^*\text{NH}_3$ . We can see that, over the  $\text{Cu}_2$  DAC, the protonation of  ${}^*\text{H}_2\text{NO}$  can firstly follow the N-consecutive mechanism to form  ${}^*\text{H}_2\text{NOH}$  (Fig. 5a) and then transforms into an O-enzymatic mechanism to form the first product  $\text{H}_2\text{O}$ . Interestingly,  ${}^*\text{H}_2\text{NO}$  species can also continuously follow the N-consecutive mechanism to form  ${}^*\text{ONH}_3$  that binds on the Cu site by an O–Cu bond, which firstly forms the product  $\text{NH}_3$  and leaves the  ${}^*\text{O}$  on the active site (Fig. 5b). The left  ${}^*\text{O}$  over the  $\text{Cu}_2$  DAC can be easily removed with small  $\Delta G$  under ambient conditions *via* the protonation process:  ${}^*\text{O} \rightarrow {}^*\text{OH} \rightarrow {}^* + \text{H}_2\text{O}$ . However, for  $\text{VCr}$ ,  $\text{VMn}$ ,  $\text{VFe}$ ,  $\text{VCu}$ , and  $\text{CrMn}$  DACs, the high  $\Delta G$  values ( $>0.8$  eV) of  ${}^*\text{OH} \rightarrow {}^* + \text{H}_2\text{O}$  induce the poisoning of active sites, despite the low  $\Delta G$  values for the hydrogenation step of  ${}^*\text{NO}$ , and  ${}^*\text{NH}_2$ , and the other steps (Fig. S5†). These results well reveal that our screening criterion is effective and straightforward for NORR activity towards  $\text{NH}_3$  and the  $\text{Cu}_2$  DAC possesses the highest electrocatalytic activity with the lowest  $\Delta G$  of  $0.30$  eV for the PDS ( $U_L = -0.30$  V).

To gain insight into the high electrocatalytic activity of the  $\text{Cu}_2$  DAC for the NORR, we revealed the intrinsic nature of the descriptor based on the d-orbital features of metal DACs, which may play an important role in the chemical and electrocatalytic activity. Based on the charge analysis of the scaling relationship with adsorption properties and free energy changes (for the details and results, see Note S4 with Fig. S14 in the ESI†) from 28 M1M2@NG DAC systems, here we found that the points for Cu-based DACs with more d electrons are concentrated in the region of higher electrocatalytic activity, though those for V and Cr-based DACs with fewer d electrons are relatively scattered in the region of lower electrocatalytic activity (Fig. 5c). This suggests that Cu-based DACs have more d electrons and thus higher electrocatalytic activity while V and Cr-based DACs with fewer d electrons induce their higher chemical activity (lower electrocatalytic activity), as observed elsewhere.<sup>5,33</sup> Thus, within reasonable limits, the  $N_{\text{d-orbital}}$  can be a simple and approximate descriptor to evaluate the electrocatalytic activity of current DAC systems for the NORR, the determination of which does not need DFT calculations.

The classical Sabatier principle in catalysis determines that the adsorption energy of the reactants should be moderate. We also analyzed the appropriate affinity between  ${}^*\text{NO}$  and the  $\text{Cu}_2$  DAC using the charge density difference (CDD) and partial density of states (PDOS), as shown in Fig. 5d. The adsorption and activation of NO over metal catalysts depend on the

“acceptance–donation” mechanism,<sup>20</sup> which denotes that the metal–NO bond formation stems from the electron acceptance of empty metal-d orbitals from the NO- $\sigma$  orbitals, and the elongation/activation of the N–O bond derives from the electron donation of metal-d orbitals to NO- $\pi^*$  orbitals. This “acceptance–donation” mechanism can be confirmed from the CDD of  ${}^*\text{NO}$  over the  $\text{Cu}_2$  DAC, where electron redistribution occurs upon NO adsorption with electron accumulation (purple region) and depletion (yellow region). Thus, the cooperation and reorganization of unoccupied and occupied d-orbitals of Cu-dimer activate the  ${}^*\text{NO}$ . We can find the electronic state hybridization between  $\text{Cu}_2$ -d (purple) and NO-sp (blue) orbitals from the PDOS upon NO adsorption on the  $\text{Cu}_2$  DAC. The d– $\pi^*$  orbital hybridization near the Fermi level indicates the activation of  ${}^*\text{NO}$ , which induces low  $\Delta G$  for the hydrogenation of  ${}^*\text{NO}$  to from  ${}^*\text{HNO}$ .

On the basis of pivotal NORR performance, it is necessary to explore multifunctional electrocatalysts that can also promote the electroreduction of  $\text{NO}_3^-$  and  $\text{NO}_2^-$  species to realize the  $\text{NO}_x\text{RR}$  towards  $\text{NH}_3$  by protonation. To conduct the electrocatalytic  $\text{NO}_3\text{RR}$  and  $\text{NO}_2\text{RR}$  on catalysts,  $\text{NO}_3^-$  and  $\text{NO}_2^-$  species are expected to be adsorbed over the  $\text{Cu}_2$  DAC, in view of the  $\text{NO}_3^-$  affinity of Cu surfaces.<sup>65</sup> We found that the  $\text{Cu}_2$  DAC possesses moderate affinity for  $\text{NO}_3^-$  and  $\text{NO}_2^-$  species (Fig. 6a), which stems from the electron donation of the  $\text{Cu}_2$  DAC to adsorbates with  $0.78$  and  $0.66$  electrons, respectively. Through free energy correction for the most stable  ${}^*\text{NO}_3$  and  ${}^*\text{NO}_2$  over the  $\text{Cu}_2$  DAC, we obtained the  $\Delta G$  ( ${}^*\text{NO}_3$ ) and  $\Delta G$  ( ${}^*\text{NO}_2$ ) as  $-0.73$  and  $-0.90$  eV, smaller than that for  ${}^*\text{H}$  ( $0.79$  eV). From the CDD results, it was found that  $\pi^*$  antibonding orbitals of  $\text{NO}_3^-$  and  $\text{NO}_2^-$  species accept electrons from the  $\text{Cu}_2$  DAC, yielding the elongation of the N–O bond and activation of  $\text{NO}_3^-$  and  $\text{NO}_2^-$  species. Therefore,  ${}^*\text{NO}_3$  is promoted to accept the hydrogenation of O atoms to in turn generate  ${}^*\text{NO}_2$  and  ${}^*\text{NO}$ . And  ${}^*\text{NO}_2$  is by means of two steps of hydrogenation to generate the  ${}^*\text{NO}$ , then following by NORR to form the final product  $\text{NH}_3$ . The corresponding  $\Delta G_{\text{max}}$  ( $U_L$ ) for the  $\text{NO}_3\text{RR}$  to  $\text{NH}_3$  (Fig. 6b) and the  $\text{NO}_2\text{RR}$  to  $\text{NH}_3$  (Fig. 6c) is  $0.36$  ( $-0.36$ ) and  $0.32$  eV ( $-0.32$  V), comparable with  $0.30$  eV ( $-0.30$  V) of the NORR to  $\text{NH}_3$ , revealing high  $\text{NO}_x\text{RR}$  activity with multifunctional electrocatalytic ability of the  $\text{Cu}_2$  DAC.

We also performed the screening strategy on 4d (Rh, Pd, and Ag) and 5d (Ir, Pt and Au) late transition-metal based homonuclear DACs to search for suitable electrocatalysts for the  $\text{NO}_x\text{RR}$ , because these metal atoms have more d-orbital electrons with potentially high electrocatalytic activity. Through firstly the screening processes for NORR electrocatalysts, the DAC of  $\text{Ag}_2@NG$  was identified as the best one due to its small  $\Delta G$  of the potential-determining step ( $0.14$  eV) and high  $\text{NH}_3$  selectivity (Table S1†). The free energy diagrams for the NORR towards  $\text{NH}_3$  over the  $\text{Ag}_2$  DAC *via* the most relevant mechanism are calculated (Fig. S6a†) and the corresponding structures of key steps along the reaction pathways are presented in Fig. S7.† Next, we obtained  $\Delta G$  ( ${}^*\text{NO}_3$ ) and  $\Delta G$  ( ${}^*\text{NO}_2$ ) as  $-0.73$  and  $-0.74$  eV, also smaller than that for  ${}^*\text{H}$  ( $0.86$  eV). The protonation of  $\text{NO}_3^-$  and  $\text{NO}_2^-$  species to  $\text{NH}_3$  was studied (Fig. S6b and c†) and the corresponding  $\Delta G_{\text{max}}$  ( $U_L$ ) for the  $\text{NO}_2\text{RR}$  and

$\text{NO}_3\text{RR}$  to  $\text{NH}_3$  is 0.14 (−0.14) and 0.23 eV (−0.23 V), comparable with its electrocatalytic activity for the NORR to  $\text{NH}_3$ . Moreover, the result of deduced  $\text{Ag}_2\text{@NG}$  is added in Fig. 5c, and is located

near the region of high electrocatalytic activity. This confirms that the  $\text{Ag}_2$  DAC (Ag and Cu metal elements belong to the same group with more d-orbital electrons) also possesses high  $\text{NO}_x\text{RR}$

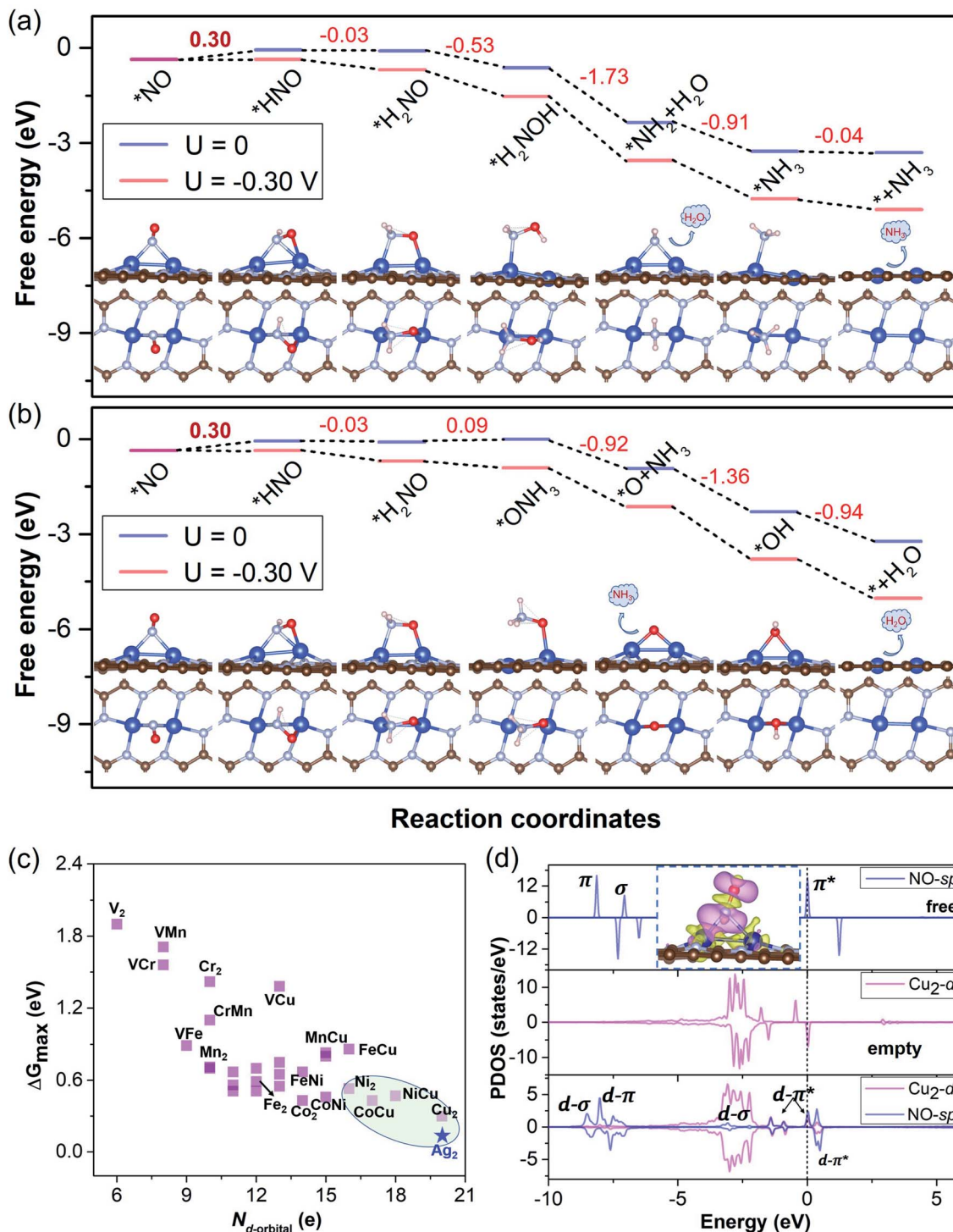


Fig. 5 (a and b) The free energy diagrams for the NORR towards  $\text{NH}_3$  over the  $\text{Cu}_2$  DAC via the two most relevant mechanisms. The corresponding free energy changes and structures of the key steps along the reaction pathways are presented and the  $\Delta G_{\max}$  values of the PDS are in bold. (c) The  $\Delta G_{\max}$  of the NORR versus the total number of d-orbital valence electrons ( $N_{d\text{-orbital}}$ ) of free metal-dimer atoms (data from 28 M1M2@NG DAC candidates ( $\text{M}_1/\text{M}_2 = \text{V, Cr, Mn, Fe, Co, Ni, and Cu}$ )). (d) The PDOS with orbital interaction for the  $\text{Cu}_2$  DAC, including the NO-sp orbitals for free NO molecules (blue), metal-d orbitals for  $\text{Cu}_2\text{@NG}$  without NO adsorption (purple), and metal-d orbitals and NO-sp orbitals for  $\text{Cu}_2\text{@NG}$  with NO adsorption, respectively. The Fermi level was set to 0. The inset shows the CDD ( $0.002\text{ e}\text{\AA}^{-3}$ ) for  $^*\text{NO}$  over the  $\text{Cu}_2$  DAC. The purple and yellow maps in the CDD denote electron accumulation and depletion, respectively.

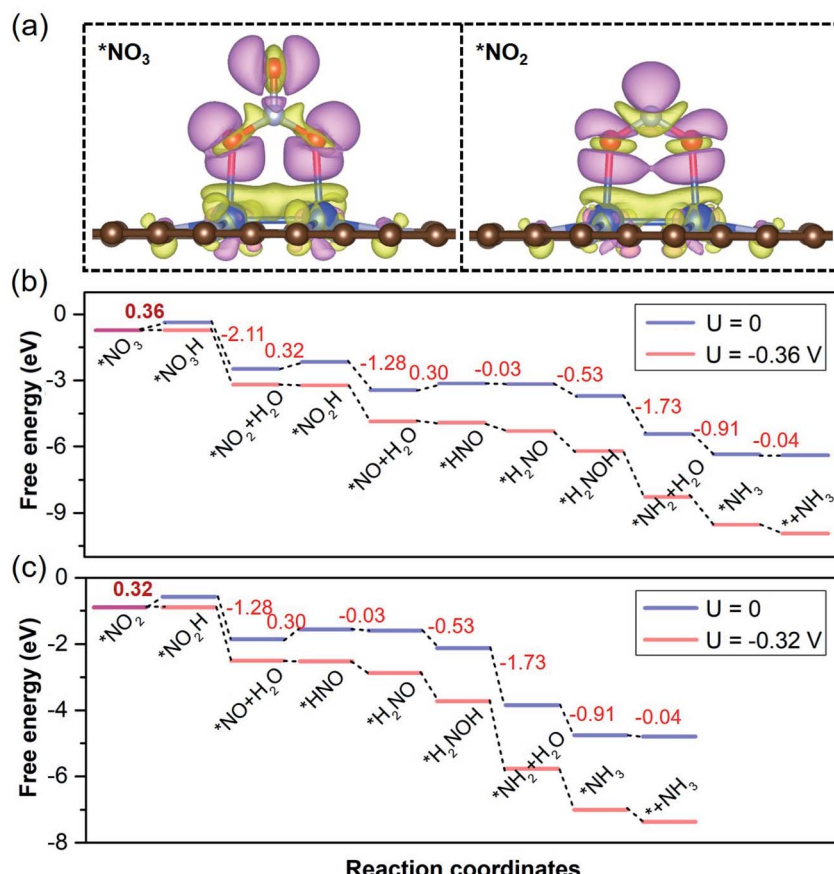


Fig. 6 (a) The most stable configurations with the CDD ( $0.002 \text{ e } \text{\AA}^{-3}$ ) for  $*\text{NO}_3$  and  $*\text{NO}_2$  over the  $\text{Cu}_2$  DAC. The purple and yellow maps in the CDD denote electron accumulation and depletion, respectively. (b) The free energy diagrams for the  $\text{NO}_3\text{RR}$  towards  $\text{NH}_3$  over the  $\text{Cu}_2$  DAC. (c) The free energy diagrams for the  $\text{NO}_2\text{RR}$  towards  $\text{NH}_3$  over the  $\text{Cu}_2$  DAC. In (b) and (c), the corresponding free energy changes of the key steps along the reaction pathway are presented and the  $\Delta G_{\text{max}}$  values of PDS are in bold.

activity with multifunctional electrocatalytic ability and again shows that our proposed screening strategy is feasible and efficient.

## 4. Conclusions

In summary, to investigate the multifunctional electrocatalytic ability of DACs for the  $\text{NO}_x\text{RR}$  towards  $\text{NH}_3$ , we firstly investigated the electrocatalytic activity of 28 DACs for the NORR by using the proposed strategy based on a first-principles screening method, which consists of the steps of “stability of catalyst”, “NO adsorption”, “NORR activity”, and “ $\text{NH}_3$  selectivity”. Specifically, the “NORR activity” criterion includes two steps of key hydrogenation processes, *i.e.*, (1)  $*\text{NO} \rightarrow *\text{NOH}/*\text{HNO}$  and (2)  $*\text{NH}_2 \rightarrow *\text{NH}_3$  and  $*\text{OH} \rightarrow * + \text{H}_2\text{O}$ , instead of considering the free energy changes for entire reaction steps. Through screening, our results reveal that the  $\text{Cu}_2@\text{NG}$  DAC is an excellent NORR electrocatalyst towards  $\text{NH}_3$  with a rather low limiting potential of  $-0.30$  V and great  $\text{NH}_3$  selectivity, while its high electrocatalytic activity is also reflected in the  $\text{NO}_2\text{RR}$  ( $-0.32$  V) and  $\text{NO}_3\text{RR}$  ( $-0.36$  V) to identify the multifunctional electrocatalytic ability of  $\text{Cu}_2@\text{NG}$ . We also find a simple

descriptor of the total number of metal-dimer d-orbital valence electrons for electrocatalytic activity. The binding affinity of NO is deeply explained by the physical mechanism including the “acceptance–donation” mechanism and orbital interaction between the active metal of the catalyst and NO. The proposed strategy helps us to find another  $\text{NO}_x\text{RR}$  multifunctional electrocatalyst from 4d and 5d late transition-metal based DACs ( $\text{Ag}_2@\text{NG}$ ). Our work effectively optimizes the screening strategy for the exploring of  $\text{NO}_x\text{RR}$  multifunctional electrocatalysts and gives an in-depth insight into the atomic mechanisms of  $\text{NO}_x$  electroreduction.

## Conflicts of interest

The authors declare no competing financial interest.

## Acknowledgements

This work is supported by the National Natural Science Foundation of China (Grant No. 12074099) and the Program for Science & Technology Innovation Talents in Universities of Henan Province (Grant No. 20HASTIT028).

## References

1 C. Ling, X. Niu, Q. Li, A. Du and J. Wang, *J. Am. Chem. Soc.*, 2018, **140**, 14161–14168.

2 X.-F. Li, Q.-K. Li, J. Cheng, L. Liu, Q. Yan, Y. Wu, X.-H. Zhang, Z.-Y. Wang, Q. Qiu and Y. Luo, *J. Am. Chem. Soc.*, 2016, **138**, 8706–8709.

3 T. Wang, Q. Liu, T. Li, S. Lu, G. Chen, X. Shi, A. M. Asiri, Y. Luo, D. Ma and X. Sun, *J. Mater. Chem. A*, 2021, **9**, 884–888.

4 C. Choi, S. Back, N.-Y. Kim, J. Lim, Y.-H. Kim and Y. Jung, *ACS Catal.*, 2018, **8**, 7517–7525.

5 D. Ma, Y. Wang, L. Liu and Y. Jia, *Phys. Chem. Chem. Phys.*, 2021, **23**, 4018–4029.

6 C. Liu, Q. Li, C. Wu, J. Zhang, Y. Jin, D. R. MacFarlane and C. Sun, *J. Am. Chem. Soc.*, 2019, **141**, 2884–2888.

7 J. Long, S. Chen, Y. Zhang, C. Guo, X. Fu, D. Deng and J. Xiao, *Angew. Chem.*, 2020, **132**, 9798–9805.

8 Y. Li, S. Xiao, X. Li, C. Chang, M. Xie, J. Xu and Z. Yang, *Mater. Today Phys.*, 2021, **19**, 100431.

9 Y. Zeng, C. Priest, G. Wang and G. Wu, *Small Methods*, 2020, **4**, 2000672.

10 J. Sun, D. Alam, R. Daiyan, H. Masood, T. Zhang, R. Zhou, P. J. Cullen, E. C. Lovell, A. Jalili and R. Amal, *Energy Environ. Sci.*, 2021, **14**, 865–872.

11 L. Li, C. Tang, X. Cui, Y. Zheng, X. Wang, H. Xu, S. Zhang, T. Shao, K. Davey and S. Qiao, *Angew. Chem.*, 2021, **133**, 2–9.

12 P. Gao, Z. Xue, S. Zhang, D. Xu, G. Zhai, Q. Li, J. Chen and X. Li, *Angew. Chem.*, 2021, **133**, 20879–20884.

13 R. Daiyan, T. Tran-Phu, P. Kumar, K. Iputera, Z. Tong, J. Leverett, M. H. A. Khan, A. Asghar Esmailpour, A. Jalili, M. Lim, A. Tricoli, R.-S. Liu, X. Lu, E. Lovell and R. Amal, *Energy Environ. Sci.*, 2021, **14**, 3588–3598.

14 H. Wan, A. Bagger and J. Rossmeisl, *Angew. Chem. Int. Ed.*, 2021, **60**, 21966–21972.

15 M. Duca and M. T. M. Koper, *Energy Environ. Sci.*, 2012, **5**, 9726–9742.

16 B. Qiao, A. Wang, X. Yang, L. F. Allard, Z. Jiang, Y. Cui, J. Liu, J. Li and T. Zhang, *Nat. Chem.*, 2011, **3**, 634–641.

17 Z. Wang, J. Zhao, J. Wang, C. R. Cabrera and Z. Chen, *J. Mater. Chem. A*, 2018, **6**, 7547–7556.

18 A. Wu, J. Yang, B. Xu, X.-Y. Wu, Y. Wang, X. Lv, Y. Ma, A. Xu, J. Zheng, Q. Tan, Y. Peng, Z. Qi, H. Qi, J. Li, Y. Wang, J. Harding, X. Tu, A. Wang, J. Yan and X. Li, *Appl. Catal. B*, 2021, **299**, 120667.

19 Q. Wu, B. Huang, Y. Dai, Y. Ma and T. Heine, ArXiv Prepr. arXiv211001947, 2021.

20 H. Niu, Z. Zhang, X. Wang, X. Wan, C. Kuai and Y. Guo, *Small*, 2021, **17**, 2102396.

21 L. Lv, Y. Shen, J. Liu, X. Meng, X. Gao, M. Zhou, Y. Zhang, D. Gong, Y. Zheng and Z. Zhou, *J. Phys. Chem. Lett.*, 2021, **12**, 11143–11150.

22 H. Niu, Z. Zhang, X. Wang, X. Wan, C. Shao and Y. Guo, *Adv. Funct. Mater.*, 2021, **31**, 2008533.

23 Y. Li, Q. Zhang, C. Li, H.-N. Fan, W.-B. Luo, H.-K. Liu and S.-X. Dou, *J. Mater. Chem. A*, 2019, **7**, 22242–22247.

24 W. Ren, X. Tan, W. Yang, C. Jia, S. Xu, K. Wang, S. C. Smith and C. Zhao, *Angew. Chem. Int. Ed.*, 2019, **58**, 6972–6976.

25 Y. Zhao, K. R. Yang, Z. Wang, X. Yan, S. Cao, Y. Ye, Q. Dong, X. Zhang, J. E. Thorne, L. Jin, K. L. Materna, A. Trimpalis, H. Bai, S. C. Fakra, X. Zhong, P. Wang, X. Pan, J. Guo, M. Flytzani-Stephanopoulos, G. W. Brudvig, V. S. Batista and D. Wang, *Proc. Natl. Acad. Sci. U. S. A.*, 2018, **115**, 2902.

26 Z. He, K. He, A. W. Robertson, A. I. Kirkland, D. Kim, J. Ihm, E. Yoon, G.-D. Lee and J. H. Warner, *Nano Lett.*, 2014, **14**, 3766–3772.

27 C. Wu, X. Zhang, Z. Xia, M. Shu, H. Li, X. Xu, R. Si, A. I. Rykov, J. Wang, S. Yu, S. Wang and G. Sun, *J. Mater. Chem. A*, 2019, **7**, 14001–14010.

28 T. He, A. R. P. Santiago, Y. Kong, M. A. Ahsan, R. Luque, A. Du and H. Pan, *Small*, 2021, 2106091.

29 Y. Cheng, S. He, J.-P. Veder, R. De Marco, S. Yang and S. Ping Jiang, *ChemElectroChem*, 2019, **6**, 3478–3487.

30 X. Lv, W. Wei, B. Huang, Y. Dai and T. Frauenheim, *Nano Lett.*, 2021, **21**, 1871–1878.

31 L. Zhang, G. Fan, W. Xu, M. Yu, L. Wang, Z. Yan and F. Cheng, *Chem. Commun.*, 2020, **56**, 11957–11960.

32 H. Li, Z. Zhao, Q. Cai, L. Yin and J. Zhao, *J. Mater. Chem. A*, 2020, **8**, 4533–4543.

33 X. Guo, J. Gu, S. Lin, S. Zhang, Z. Chen and S. Huang, *J. Am. Chem. Soc.*, 2020, **142**, 5709–5721.

34 D. Ma, Z. Zeng, L. Liu, X. Huang and Y. Jia, *J. Phys. Chem. C*, 2019, **123**, 19066–19076.

35 Z. W. Chen, J.-M. Yan and Q. Jiang, *Small Methods*, 2019, **3**, 1800291.

36 Z.-Y. Wu, M. Karamad, X. Yong, Q. Huang, D. A. Cullen, P. Zhu, C. Xia, Q. Xiao, M. Shakouri, F.-Y. Chen, J. Y. Kim, Y. Xia, K. Heck, Y. Hu, M. S. Wong, Q. Li, I. Gates, S. Siahrostami and H. Wang, *Nat. Commun.*, 2021, **12**, 2870.

37 G.-F. Chen, Y. Yuan, H. Jiang, S.-Y. Ren, L.-X. Ding, L. Ma, T. Wu, J. Lu and H. Wang, *Nat. Energy*, 2020, **5**, 605–613.

38 P. Li, Z. Jin, Z. Fang and G. Yu, *Energy Environ. Sci.*, 2021, **14**, 3522–3531.

39 W. Ye, S. Chen, Y. Lin, L. Yang, S. Chen, X. Zheng, Z. Qi, C. Wang, R. Long, M. Chen, J. Zhu, P. Gao, L. Song, J. Jiang and Y. Xiong, *Chem*, 2019, **5**, 2865–2878.

40 J. Wang, Z. Huang, W. Liu, C. Chang, H. Tang, Z. Li, W. Chen, C. Jia, T. Yao, S. Wei, Y. Wu and Y. Li, *J. Am. Chem. Soc.*, 2017, **139**, 17281–17284.

41 J. Wang, W. Liu, G. Luo, Z. Li, C. Zhao, H. Zhang, M. Zhu, Q. Xu, X. Wang, C. Zhao, Y. Qu, Z. Yang, T. Yao, Y. Li, Y. Lin, Y. Wu and Y. Li, *Energy Environ. Sci.*, 2018, **11**, 3375–3379.

42 X. Han, X. Ling, D. Yu, D. Xie, L. Li, S. Peng, C. Zhong, N. Zhao, Y. Deng and W. Hu, *Adv. Mater.*, 2019, **31**, 1905622.

43 T. Deng, C. Cen, H. Shen, S. Wang, J. Guo, S. Cai and M. Deng, *J. Phys. Chem. Lett.*, 2020, **11**, 6320–6329.

44 J. P. Perdew, K. Burke and M. Ernzerhof, *Phys. Rev. Lett.*, 1996, **77**, 3865.

45 G. Kresse and J. Furthmüller, *Phys. Rev. B: Condens. Matter Mater. Phys.*, 1996, **54**, 11169.

46 G. Kresse and J. Furthmüller, *Comput. Mater. Sci.*, 1996, **6**, 15–50.

47 S. Grimme, J. Antony, S. Ehrlich and H. Krieg, *J. Chem. Phys.*, 2010, **132**, 154104.

48 A. A. Peterson, F. Abild-Pedersen, F. Studt, J. Rossmeisl and J. K. Nørskov, *Energy Environ. Sci.*, 2010, **3**, 1311–1315.

49 J. K. Nørskov, J. Rossmeisl, A. Logadottir, L. Lindqvist, J. R. Kitchin, T. Bligaard and H. Jónsson, *J. Phys. Chem. B*, 2004, **108**, 17886–17892.

50 J. Rossmeisl, A. Logadottir and J. K. Nørskov, *Chem. Phys.*, 2005, **319**, 178–184.

51 <http://webbook.nist.gov/chemistry/>.

52 V. Wang, N. Xu, J.-C. Liu, G. Tang and W.-T. Geng, *Comput. Phys. Commun.*, 2021, **267**, 108033.

53 Y. Wang, X. Qin and M. Shao, *J. Catal.*, 2021, **400**, 62–70.

54 G. Brancato, N. Rega and V. Barone, *J. Chem. Phys.*, 2008, **128**, 144501.

55 K. Mathew, R. Sundararaman, K. Letchworth-Weaver, T. A. Arias and R. G. Hennig, *J. Chem. Phys.*, 2014, **140**, 084106.

56 G. J. Martyna, M. L. Klein and M. Tuckerman, *J. Chem. Phys.*, 1992, **97**, 2635–2643.

57 L. Zhang, J. Liang, Y. Wang, T. Mou, Y. Lin, L. Yue, T. Li, Q. Liu, Y. Luo, N. Li, B. Tang, Y. Liu, S. Gao, A. A. Alshehri, X. Guo, D. Ma and X. Sun, *Angew. Chem.*, 2021, **133**, 1–7.

58 X. Peng, Y. Mi, H. Bao, Y. Liu, D. Qi, Y. Qiu, L. Zhuo, S. Zhao, J. Sun, X. Tang, J. Luo and X. Liu, *Nano Energy*, 2020, **78**, 105321.

59 D. Kim, D. Shin, J. Heo, H. Lim, J.-A. Lim, H. M. Jeong, B.-S. Kim, I. Heo, I. Oh, B. Lee, M. Sharma, H. Lim, H. Kim and Y. Kwon, *ACS Energy Lett.*, 2020, **5**, 3647–3656.

60 S. L. Foster, S. I. P. Bakovic, R. D. Duda, S. Maheshwari, R. D. Milton, S. D. Minteer, M. J. Janik, J. N. Renner and L. F. Greenlee, *Nat. Catal.*, 2018, **1**, 490–500.

61 Y. Xiao and C. Shen, *Small*, 2021, 2100776.

62 Q. Wu, H. Wang, S. Shen, B. Huang, Y. Dai and Y. Ma, *J. Mater. Chem. A*, 2021, **9**, 5434–5441.

63 J. Zhao and Z. Chen, *J. Am. Chem. Soc.*, 2017, **139**, 12480–12487.

64 S. Chatterjee, C. Griego, J. L. Hart, Y. Li, M. L. Taheri, J. Keith and J. D. Snyder, *ACS Catal.*, 2019, **9**, 5290–5301.

65 T. Hu, C. Wang, M. Wang, C. M. Li and C. Guo, *ACS Catal.*, 2021, 14417–14427.